aerospace

MDPI

Article

Fatigue Life Prediction for 2060 Aluminium–Lithium Alloy with Impact Damage

Lei Li [1,2,3], Xiongfei Li [4], Zhixin Zhan [4,*], Weiping Hu [4] and Qingchun Meng [4]

[1] State Key Laboratory of Mechanics and Control of Mechanical Structures, Nanjing University of Aeronautics and Astronautics, Nanjing 210016, China
[2] Shanghai Aircraft Design & Research Institute, Commercial Aircraft Corporation of China, Shanghai 201210, China
[3] State Key Laboratory of Airliner Integration Technology and Flight Simulation, Commercial Aircraft Corporation of China, Shanghai 201210, China
[4] National Key Laboratory of Strength and Structural Integrity, School of Aeronautic Science and Engineering, Beihang University, Beijing 100191, China
* Correspondence: zzxupc@163.com

Abstract: The paper investigates the issue of post-impact fatigue damage of the 2060 aluminium–lithium alloy, a representative material of third-generation aluminium–lithium alloys extensively employed in the fuselage of C919 aircraft due to its notable attributes of high specific stiffness and strength. Initial impact damage is identified utilizing a residual stress–strain field obtained from a quasi-static simulation. Then, the continuum damage mechanics approach is applied to predict the fatigue life of the impacted 2060 aluminium–lithium alloy plates accounting for the combined effects of residual stress, plastic damage, and fatigue loading. A comparative analysis between calculated and experimental results is conducted to validate the efficacy of the proposed methodology.

Keywords: aluminium–lithium alloy; fatigue life; damage mechanics; residual stress; impact

Citation: Li, L.; Li, X.; Zhan, Z.; Hu, W.; Meng, Q. Fatigue Life Prediction for 2060 Aluminium–Lithium Alloy with Impact Damage. *Aerospace* **2024**, *11*, 536. https://doi.org/10.3390/aerospace11070536

Academic Editor: Cheng-Wei Fei

Received: 10 May 2024
Revised: 21 June 2024
Accepted: 25 June 2024
Published: 29 June 2024

1. Introduction

Aluminium–lithium alloys have gained widespread attention in aerospace applications where high weight reduction is required for higher specific strength and specific stiffness than conventional aluminium alloys [1–3]. The third generation of 2060 aluminium–lithium alloys that have emerged in recent years have exhibited significant improvements in strength and toughness, surpassing the performance of the second-generation aluminium–lithium alloys [4,5]. Consequently, the integration of the 2060 aluminium–lithium alloy has emerged as a pivotal choice for aircraft fuselage wall panel materials [6–8].

Aircraft are subjected to aerodynamic loads, sudden wind loads, and landing impact loads in service, which will produce alternating stresses at the material point and cause fatigue damage. Fatigue failure is a gradual process of damage accumulation under cyclic stress or strain until crack initiation or fracture. Fatigue failure is the most common form of mechanical and structural failure, and it occurs even if the cyclic stresses in components are much less than the strength limit of the materials, which is distinctly different from static failure [9–11]. Moreover, fatigue damage typically exhibits localized traits, with alterations in local conditions exerting pronounced effects on fatigue life. During aircraft operations, low-energy impactors such as hailstones and debris often hit the aircraft surfaces, resulting in impact damage, the formation of pit defects on the surfaces of the aircraft, and the generation of localized stress concentrations, which greatly reduce the fatigue life of the aircraft structures [12,13]. Therefore, it is essential to conduct post-impact fatigue life studies on the new generation of aluminium–lithium alloys used in aircraft to provide experimental data and theoretical support for the maintenance of aircraft structures.

Numerous studies indicate that pre-impact significantly affects the fatigue properties of materials in two primary ways. One involves the detrimental effect of stress concentration induced by post-impact geometric changes, and the other pertains to the influence of the residual stress–strain field after impact [14,15]. The plastic zone around the impact crater retards crack propagation [14,15], while the residual stresses alter the mean stress and stress ratio of the subsequent fatigue loads, thus affecting the fatigue life [16]. In general, residual compressive stresses are desired to prolong fatigue life, whereas the presence of residual tensile stresses reduces fatigue life, with cracks initiating at sites of residual tensile stresses [17]. Residual stresses gradually relax during subsequent loading cycles, with the most significant stress relaxation occurring in the first loading cycle [16,18,19]. Fatigue crack nucleation mainly depends on the dent geometry induced by the impact. The zone around the impact crater is also subjected to a complex state of stress under uniaxial fatigue loading and the initiated crack propagates in a combination failure mode of type I and type III, leading to a faster rate of crack propagation [20,21].

It is also worth noting that impact energy [15,20–24], impact pit dimension [16,20], and insert shape [20,21] have an influence on the residual fatigue life, which increases the complexity of post-impact fatigue life prediction. Typically, the post-impact fatigue life decreases with increasing impact energy [15,20–23]. However, at lower impact energies, the post-impact fatigue life may exceed that under no-impact conditions due to the fortification of the dent region precipitated by the impact-induced hardening effect [21]. The damage induced by a U-shaped insert is more severe than that induced by a hemispherical insert under the same impact energy, resulting in a reduction in the life of specimens containing U-shaped impact dents [20]. In addition, as the depth of the dent increases, stress concentration intensifies, leading to a shorter fatigue life and an increase in initial impact damage [16,17,20]. The effect of dent radius on the fatigue life of a specimen containing a dent is related to the shape of the impactor when the pit depth is kept unchanged. For U-shaped foreign object impacts, the fatigue life increases with increasing dent radius, while this result is reversed for hemispherical foreign object impacts [20].

Summing up the above analyses, one can observe that pre-impact exerts a significant effect on the fatigue properties of materials. First, pre-impact causes initial impact damage to the materials. It is a critical issue to accurately calculate the initial damage when predicting post-impact fatigue life. In addition, the stress–strain response of the specimen with an impact crater under fatigue loading is very different from that of the specimen without impact due to the change of geometry and the residual stress–strain field formed after the impact, which also brings difficulties to the calculation of fatigue life after impact. Various methods have been used to predict post-impact fatigue life. The nominal stress method is a simple method of predicting high cycle fatigue life using the *S-N* curves of materials. Chen et al. [20] used ABAQUS 2020 /Explicit to obtain the strain distribution on the concave surface of specimens with impact craters and then predicted the post-impact fatigue life of 2024-T3 plates using Fe-safe, which is a platform for life prediction based on the *S-N* curves of materials. Based on the post-impact fatigue test results of CFRP/Al-bonded joints and the Weibull distribution of two parameters, Liu et al. [15] acquired the *S-N* curves of CFRP/Al-bonded joints at different confidence levels, which can be used to predict the post-impact fatigue life of CFRP/Al-bonded joints. However, a large number of tests are often required to obtain fatigue curves for materials under different operating conditions. Fracture mechanics provides the theoretical foundation for investigating crack propagation and is also utilized in the prediction of post-impact fatigue life. Cheng et al. [14] proposed a crack propagation model considering load interactions and low-velocity impact damage to investigate the crack propagation behaviour of impact-damaged 7075-T62 aluminium alloy sheets under block-spectrum loading. Nevertheless, the fracture mechanics approach confines its scope to the crack propagation phase, disregarding the initiation phase of crack formation. Within the framework of continuum damage mechanics, damage is conceptualized as an internal state variable of materials. The damage-coupled constitutive equations and damage evolution equations have been derived on the basis of thermodynamic princi-

ples to capture and describe the whole process of materials from deformation, and damage generation to fatigue failure, which are widely used in structural fatigue analysis [25–29]. Zhan et al. [16] obtained the residual stress–strain and impact damage after impact through a quasi-static analysis and then predicted the fatigue life of specimens with impact pits based on the continuum damage mechanics method by considering the initial impact damage, residual stress relaxation, and elastic–plastic fatigue damage. Yang et al. [17] proposed a novel damage evolution equation considering the detrimental effect of impact pits to predict the post-impact fatigue life of specimens and hole plates with impact pits, and the prediction results aligned well with the test results.

In the present study, the damage mechanics approach was taken to investigate the post-impact fatigue issue of the 2060 aluminium–lithium alloy. First, impact tests on the 2060 aluminium alloy plate specimens were carried out on a drop hammer impact tester, followed by fatigue tests on the specimens with impact pits, and the test data were used for comparison with the finite element results. Then, a quasi-static numerical simulation of the impact pit formation was performed on the ABAQUS platform to obtain the residual stress field and plastic strain field after the impact. Utilizing Lemaitre's damage model, the initial damage caused by plastic deformation around the impact pit was calculated. Finally, Shen's multiaxial fatigue damage evolution model was adopted to calculate the fatigue life of the specimens with initial impact damage. The calculated results were compared with the test results to verify the validity of the methodology adopted in this study.

2. Experiments

2.1. Material and Specimen

The material studied in this paper is the 2060-T8E30 aluminium–lithium alloy, which has improved fracture toughness and corrosion resistance compared to the conventional 2024 aluminium alloy materials; its chemical composition is listed in Table 1 [30]. Figure 1 shows the monotonic tensile curve of the 2060 aluminium alloy, from which the elastic modulus, yield stress, and strength limit of the material can be obtained as listed in Table 2. The specimen is a 2 mm thick plate, with its geometric configuration and dimensions depicted in Figure 2.

Table 1. Typical chemical composition of 2060-T8E30 aluminium–lithium alloy.

Cu	Li	Mg	Mn	Zn	Zr	Si	Fe	Ag	Al
3.95	0.75	0.85	0.30	0.35	0.1	0.05	0.07	0.5	Bal.

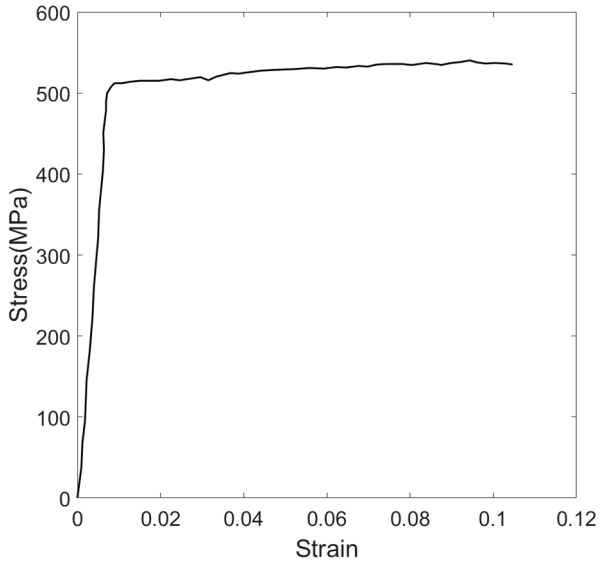

Figure 1. Stress–strain curve of 2060-T8E30 aluminium alloy under uniaxial tension.

Table 2. Static properties of 2060-T8E30 aluminium–lithium alloy.

Elastic Modulus (Gpa)	Poisson's Ratio	Yield Stress (MPa)	Ultimate Tensile Stress (Mpa)
72	0.3	501	539

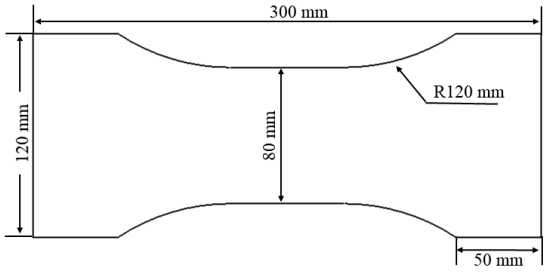

Figure 2. Geometry of the specimen.

2.2. Pre-Impact Test

In routine aircraft maintenance, the width and area of craters caused by impacts such as stones and hailstones are difficult to measure, while the depth is convenient to obtain. Therefore, the crater width was fixed during the pre-impact test and the focus was on the relationship between crater depth and fatigue life. A pit with a specified width-to-depth ratio was generated at the centre of the specimen using a steel spherical hammer with a diameter of 25.4 mm, as shown in Figure 3, where W is the width of the pit and Y is the depth of the pit. In the impact tests of this paper, W was fixed at 20 mm and the impact depth Y was 0.67 mm, 1.33 mm, and 2.00 mm for width-to-depth ratios of 30, 15, and 10, respectively.

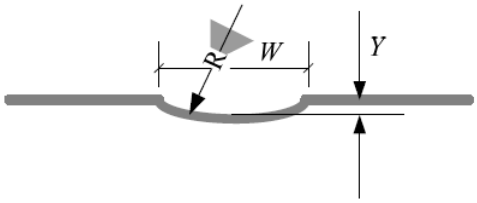

Figure 3. Schematic diagram of shape and key dimensional parameters of an impact pit.

Impact testing was conducted on a Ceast 9350 Drop Hammer Impact Tester (Figure 4). The width of the impact pit was kept constant through the application of specialized fixtures, while the impact mass was controlled by adjusting the mass of the counterweight.

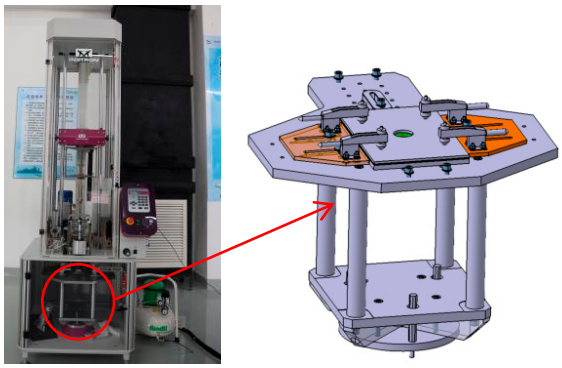

Figure 4. Ceast 9350 testing machine (The part marked in red circle is the schematic diagram of the experimental apparatus).

A discernible step formed at the periphery of the impact pit, leading to notable stress concentration. The depth of the impact pit and the magnitude of stress concentration

proportionally escalated with increasing impact energy. Concurrently, the impact induced a proliferation of micro-cracks within the specimen, as shown in Figure 5.

(**a**) (**b**) (**c**)

Figure 5. Morphology of impact pit and step, (**a**) impact pit; (**b**) step formed at the edge of the pit after impact; (**c**) step under the electron microscope.

2.3. Post-Impact Fatigue Test

After the impact test was completed, the specimen was installed on the MTS 370 material testing machine (as shown in Figure 6), and the axial constant amplitude loading fatigue test with a stress ratio of 0.06 was carried out. The crack initiation and propagation path can be clearly seen under the electron microscope, as shown in Figure 7. The main crack emerged from the micro-cracks generated by the impact, and it was easier for the main crack to nucleate and expand as the micro-cracks became denser, leading to fatal damage to the specimen. The fatigue test data are listed in Table 3. A total of four post-impact fatigue experiments were carried out at four different impact pit depths of 0 mm (without impact pit), 0.67 mm, 1.33 mm, and 2 mm, with peak loads of 36 kN, 28 kN, 25 kN, and 22 kN, respectively. The fatigue life is relatively close for the four cases, as the peak load decreased with increasing impact pit depths. It has been shown that fatigue life decreases with increasing impact pit depth for the same loading conditions [16].

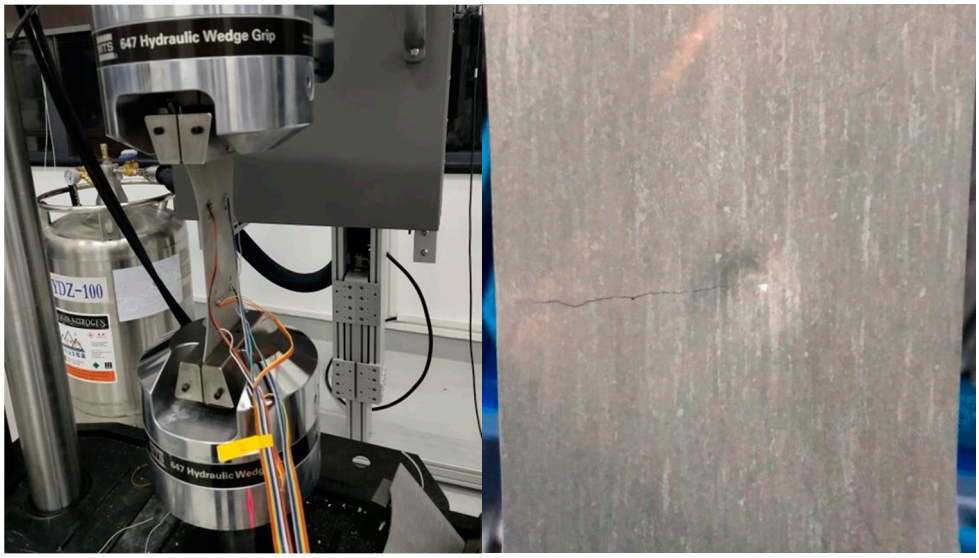

Figure 6. Fatigue testing machine and fatigue fracture morphology of a specimen with an impact pit.

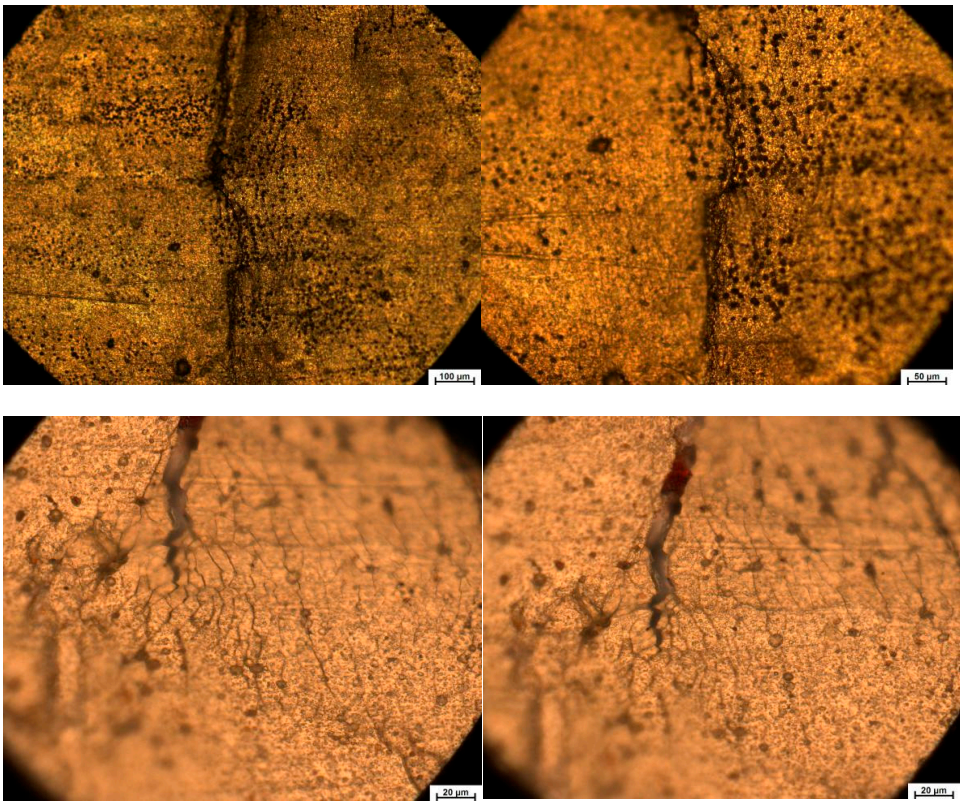

Figure 7. Electron microscope image of crack initiation point.

Table 3. Fatigue test results.

Specimen Number	Width-to-Depth Ratio	Pit Depth (mm)	Peak Load (kN)	Stress Ratio	Fatigue Life (Cycle)	Average Life (Cycle)
1	0	0	36	0.06	122,796	136,717
2	0	0	36	0.06	148,596	
3	0	0	36	0.06	147,291	
4	0	0	36	0.06	136,926	
5	0	0	36	0.06	103,351	
6	0	0	36	0.06	161,341	
7	10	2	22	0.06	134,157	170,445
8	10	2	22	0.06	161,201	
9	10	2	22	0.06	144,541	
10	10	2	22	0.06	148,523	
11	10	2	22	0.06	220,022	
12	10	2	22	0.06	203,534	
13	10	2	22	0.06	181,142	
14	15	1.33	25	0.06	204,121	163,812
15	15	1.33	25	0.06	164,038	
16	15	1.33	25	0.06	128,960	
17	15	1.33	25	0.06	133,149	
18	15	1.33	25	0.06	251,635	
19	15	1.33	25	0.06	142,279	
20	15	1.33	25	0.06	101,065	
21	15	1.33	25	0.06	185,252	

Table 3. *Cont.*

Specimen Number	Width-to-Depth Ratio	Pit Depth (mm)	Peak Load (kN)	Stress Ratio	Fatigue Life (Cycle)	Average Life (Cycle)
22	30	0.67	28	0.06	228,298	141,393
23	30	0.67	28	0.06	98,475	
24	30	0.67	28	0.06	94,998	
25	30	0.67	28	0.06	154,815	
26	30	0.67	28	0.06	168,023	
27	30	0.67	28	0.06	150,021	
28	30	0.67	28	0.06	102,587	
29	30	0.67	28	0.06	133,931	

3. Theoretical Models

3.1. Residual Stress Analysis Model

Residual stresses are usually caused by inhomogeneous plastic deformation. The stresses cease to match between the plastic zone and the surrounding elastic zone due to permanent plastic deformation, which introduces a system of residual stresses. It is necessary to combine plasticity theory and finite element methodology for residual stress analysis. In the simulation of impact, the hammer can be considered a rigid body while the specimen is regarded as an elastic–plastic body since the hardness of the hammer is much higher than that of the specimen. Impact is a typical dynamic process, featuring a rapid loading time, a significant plastic deformation, and a high strain rate. However, dynamic simulations are time-consuming, and the results may be unstable in certain scenarios. Additionally, the calculation of fatigue life following dynamic impact simulations is considerably more complex than after quasi-static impact simulations. On the other hand, the quasi-static analysis provides a more accessible and efficient method for determining the residual stress–strain field when focusing solely on the final impact response [16]. Thus, a quasi-static impact simulation is conducted in this investigation to ascertain the residual stress–strain field subsequent to the impact.

The stress–strain behaviour of the material during impact is characterized using a segmented linear plasticity model. As the impact process proceeds, large strains are first generated at the contact surface between the hammer and the specimen, and then the strain begins to spread along the contact surface. After the impact process is completed, the elastic deformation of the material is restored while the plastic deformation is irrecoverable. The plastic deformation varies at different material points, which results in a mismatch between the stresses in the plastic zone and the surrounding elastic zone, with residual stresses remaining on the surface of the specimen to maintain equilibrium.

3.2. Initial Impact Damage Analysis Model

In the framework of continuum damage mechanics, the concept of representative volume element (RVE) is first introduced to homogenize the influence of the microstructure on the mechanical properties of materials, given that both the materials and the damage are micro-discontinuous. Damage variables are then defined to describe the damage state of the materials. For isotropic materials, the damage variable can be defined as the percentage reduction in the effective bearing area of the RVE [31]:

$$D = \frac{\mathrm{d}A - \mathrm{d}\widetilde{A}}{\mathrm{d}A} = \frac{\mathrm{d}A_D}{\mathrm{d}A} \tag{1}$$

where $\mathrm{d}\widetilde{A}$ is the effective bearing area, $\mathrm{d}A$ is the cross-sectional area of RVE, and $\mathrm{d}A_D$ is the equivalent total area of micro-cavities or micro-cracks. The physical meaning of the above equation is clear; however, it is not convenient for direct application. Considering that

damage leads to a decrease in material stiffness, the damage variable can also be defined in the following more common form:

$$D = \frac{E - E_D}{E} \tag{2}$$

where E is the elastic modulus of the material without damage and E_D is the effective elastic modulus of the material with damage. The value range of D is 0~1, D = 0 represents the initial undamaged state, and D = 1 represents the final fractured state. A change in the value of D from 0 to 1 means a transition of the material from an undamaged state to a final fracture state.

When the material undergoes plastic deformation, the damage of the material is mainly dependent on the stress state and the cumulative plastic strain of the material. This damage induced by plastic deformation can be defined as elastic–plastic damage or ductile damage. Based on the theory of damage thermodynamics, Lemaitre [32] proposed the following elastoplastic damage evolution equation

$$\dot{D} = \left(\frac{\sigma_{eq}^2 R_v}{2ES(1-D)^2} \right)^m \dot{p} \tag{3}$$

$$R_v = \frac{2}{3}(1+v) + 3(1-2v)\left(\frac{\sigma_H}{\sigma_{eq}} \right)^2 \tag{4}$$

where $\dot{p}$ is the cumulative plastic strain rate, S and m are the material parameters, R_v is the stress triaxiality function, σ_{eq} represents von Mises stress, and σ_H is the hydrostatic pressure.

The damage increment for one cycle can be obtained by integrating Equation (3) over the cycle

$$\int_{cycle} \dot{D} dt = \Delta D = \left[\frac{\sigma_{eq,\max}^2 R_v}{2ES(1-D)} \right]^m \Delta p \tag{5}$$

According to Equation (5), the initial damage induced by impact can be expressed as

$$D_0 = \left[\frac{\sigma_{eq,\max}^2 R_v}{2ES} \right]^m \Delta p \tag{6}$$

The residual stress–strain field can be obtained via a quasi-static impact simulation. Then, the initial impact damage can be calculated with Equation (6).

3.3. Fatigue Damage Analysis Model

The post-impact fatigue cases studied in this paper all fall into the scope of high cycle fatigue, where the fatigue damage is mainly caused by elastic deformation. Therefore, the damage caused by plastic deformation is neglected in the analysis of post-impact fatigue problems. By assuming a reasonable dissipation potential function based on the damage mechanism of high cycle fatigue, Xiao [33] derived an elastic damage evolution equation incorporating the effect of stress amplitude and mean stress

$$\frac{\mathrm{d}D}{\mathrm{d}N} = \alpha \left(\frac{\sigma_a}{1 - n\sigma_m} \right)^m (1-D)^{-\beta} \tag{7}$$

where N represents the loading cycle; σ_a and σ_m represent stress amplitude and mean stress, respectively; and α, β, m, and n are material parameters.

Equation (7) only applies to cases where the material is under uniaxial loading, which limits its application. Shen et al. [34] extended Equation (7) to complex stress state using the concept of damage equivalent stress:

$$\frac{\mathrm{d}D}{\mathrm{d}N} = \alpha \left(\frac{\sigma_a^*}{1 - n\sigma_m^*} \right)^m (1 - D)^{-\beta} \tag{8}$$

$$\sigma_a^* = \sigma^*(\sigma_{ij,\max} - \sigma_{ij,\min})/2 \tag{9}$$

$$\sigma_m^* = sign(\sigma_m) \cdot \sigma^*(\sigma_{ij,\max} + \sigma_{ij,\min})/2 \tag{10}$$

where σ^* is damage equivalent stress with the expression of $\sigma^*(\sigma_{ij}) = \sigma_{eq} R_v^{1/2}$. $\sigma_{ij,\max}$ and $\sigma_{ij,\min}$ symbolize the stress states occurring at the peak and nadir of external loading within a single loading cycle, respectively. σ_m is defined as $\sigma_m = \frac{1}{6}(\sigma_{kk,\max} + \sigma_{kk,\min})$. Sign() represents the sign function.

4. Parameter Calibration

Equations (3) and (8) play pivotal roles in post-impact fatigue life prediction. Several material parameters in these two equations need to be calibrated using standard fatigue test data.

4.1. Calibration of the Parameters in the Plastic Damage Evolution Equation

Two parameters, S and m, in the plastic damage evolution model need to be calibrated from strain-controlled low-cycle fatigue test data. In the case where the smooth specimen is subject to uniaxial loading, Equation (3) can be expressed as

$$\frac{\mathrm{d}D}{\mathrm{d}N} = \left[\frac{\sigma_{\max}^2}{2ES(1 - D)^2} \right]^m \Delta p \tag{11}$$

where $\sigma_{\max}$ represents the maximum stress and Δp is the plastic strain increment in one loading cycle.

The low-cycle fatigue life can be obtained by integrating the damage variable D from 0 to 1:

$$N_f = \frac{1}{(2m + 1)\Delta p} \left(\frac{2ES}{\sigma_{\max}} \right)^m \tag{12}$$

For a low-cycle fatigue test with a strain ratio of -1, the plastic strain increment for one cycle Δp is two times that of the plastic strain amplitude $\Delta \varepsilon_p$; therefore, Equation (12) can also be expressed as

$$N_f = \frac{1}{2(2m + 1)\Delta \varepsilon_p} \left(\frac{2ES}{\sigma_{\max}} \right)^m \tag{13}$$

According to the cyclic stress–strain curve, the maximum stress in one loading cycle is related to the plastic strain as follows:

$$\sigma_{\max} = K \left(\frac{\Delta \varepsilon_p}{2} \right)^r \tag{14}$$

Combining Equations (13) and (14), the fatigue life can be expressed as a univariate function of the plastic strain amplitude:

$$N_f = \frac{1}{2(2m + 1)} \left(\frac{2^{1+2r} ES}{K^2} \right)^m (\Delta \varepsilon_p)^{-(1+2mr)} \tag{15}$$

In addition, the low-cycle fatigue life and the plastic strain amplitude satisfy the Coffin–Mansion relationship:

$$\frac{\Delta \varepsilon_p}{2} = \varepsilon_f' (2N_f)^{c'} \tag{16}$$

The parameters S and m can then be determined by comparing Equations (15) and (16) based on the standard low-cycle fatigue test data. The calibrated results are listed in Table 4.

Table 4. Parameters in plastic damage evolution model.

S/MPa	m
3.459	1.178

4.2. Calibration of the Parameters in the Plastic Damage Evolution Equation

Four parameters—α, β, m, and n—in the elastic damage evolution model need to be calibrated from stress-controlled high-cycle fatigue test data.

The high-cycle fatigue life of a smooth specimen can be obtained by integrating the damage variable D in Equation (7) from 0 to 1:

$$N_f = \frac{1}{\alpha(1+\beta)}\left(\frac{\sigma_a}{1-n\sigma_m}\right)^{-m} \tag{17}$$

Parameters $1/[\alpha/(1+\beta)]$ and m were determined from the data of smooth specimens with a stress ratio of -1 and parameter n was then determined from the data of smooth specimens with a stress ratio of 0. Since parameters α and β cannot be decoupled in the uniaxial stress state, they were determined by adjusting their values until the finite element calculated lives coincide well with the lives of notched specimens.

The alloy 2060-T8E30 is a newly developed material with very limited fatigue test data. The limited fatigue tests conducted suggest that the notch fatigue allowable for the 2060-T8E30 plate closely aligns with that of the 2024-T3 plate, as indicated in Table 5. Considering the lack of sufficient high-cycle fatigue data for the 2060 aluminium–lithium alloy and the similarity in notch fatigue allowables with 2024, it is assumed that variations in fatigue properties between 2024-T3 and 2060-T8E30 are solely driven by differences in a specific material parameter α. Based on this assumption, the material parameters of 2024-T3 were first calibrated using its fatigue test data, and the parameter α of 2060-T8E30 was determined by adjusting its value until the fatigue life of one 2060 smooth specimen agreed well with the test result.

Table 5. Comparison of notch allowable fatigue value between 2060 and 2024.

	Notch Fatigue Allowable Value/MPa	
Stress concentration coefficient	2060-T8E30	2024-T3
1.5	174	180
2.0	134	140
3.0	97	96.5
4.0	74	73.5

According to the material handbook, the statistical formula for the fatigue life of 2024 plate specimens is

$$\begin{cases} \log N_f = 11.1 - 3.97\log(S_{\max}(1-R)^{0.56} - 15.8) \text{ for } K_t = 1 \\ \log N_f = 9.2 - 3.33\log(S_{\max}(1-R)^{0.68} - 12.3) \text{ for } K_t = 2 \end{cases} \tag{18}$$

where, S_{max} (unit: Ksi) is the maximum nominal stress, S_{min} (unit: Ksi) is the minimum nominal stress, R is defined as S_{min}/S_{max} is the stress ratio, and N is the cycle life.

Using the above parameter calibration method, the material parameters of 2060-T8E30 are calibrated as shown in Table 6.

Table 6. Parameters in plastic damage evolution model.

α	β	m	n
5.3089×10^{-18}	7.5	5.40	2.143×10^{-4}

5. Numerical Simulation and Model Verification

The analysis of post-impact fatigue issues involves two aspects: the determination of the initial impact damage and the calculation of the fatigue life considering the combined effect of initial impact damage and impact pit. In the theory of continuum damage mechanics, material properties are related to the damage variable. Therefore, the material properties are modified accordingly after the damage variable is updated. The procedure for post-impact life prediction is shown in Figure 8, with the following steps:

1. Obtain residual stress–strain field through a quasi-static impact simulation.
2. Calculate initial impact damage according to Lemaitre's elastic–plastic damage evolution equation, shown in Equation (6).
3. The material properties are modified according to the current damage degree (as shown in Equation (19)), and the alternating stress field in one cycle is then calculated using the damage-coupled constitutive relationship.

$$E_D = E_0(1 - D) \tag{19}$$

4. The jump-in-cycle method is used in the fatigue life accumulation considering that it is very time-consuming to calculate the fatigue life cycle by cycle. It is assumed that the alternating stress–strain field is the same within a finite number of ΔN cycles and each cycle produces the same damage increment. The damage increment resulting from ΔN cycles is calculated with Equation (20). Subsequently, the damage variable and the number of loading cycles are updated. Typically, it is reasonable for ΔN to be 1–2% of the calculated fatigue life.

$$\Delta D^{(i)} = \alpha \left(\frac{\sigma_a^*}{1 - n\sigma_m^*} \right)^m (1 - D)^{-\beta} \Delta N \tag{20}$$

$$D^{(i+1)} = D^{(i)} + \Delta D^{(i)} \tag{21}$$

$$N^{(i+1)} = N^{(i)} + \Delta N \tag{22}$$

5. Repeat steps 3–4 until the damage variable of one element reaches the critical value, and the number of loading cycles at this point is the crack initiation life.

5.1. Initial Impact Damage Calculation

A quasi-static simulation of the impact process was carried out on the ABAQUS platform. The corresponding finite element model, presented in Figure 9, comprises a plate specimen and a hemispherical hammer. Due to the significantly higher stiffness of the hammer relative to the specimen, the former is modelled as a rigid body and the latter as an elastic–plastic entity. The lower surface of the specimen is fixed except for a circular surface with a diameter of 20 mm located in the centre, which is free, as shown in Figure 10. The C3D8R reduced integration element with eight nodes and one integration point was adopted in the finite element model, and the mesh size in the vicinity of the impact pit was determined to be 1 mm via mesh convergence calculation. In the simulation of the impact, the depth of the impact pit was 0.67 mm, 1.33 mm, and 1.67 mm, respectively, which is consistent with the experimental conditions.

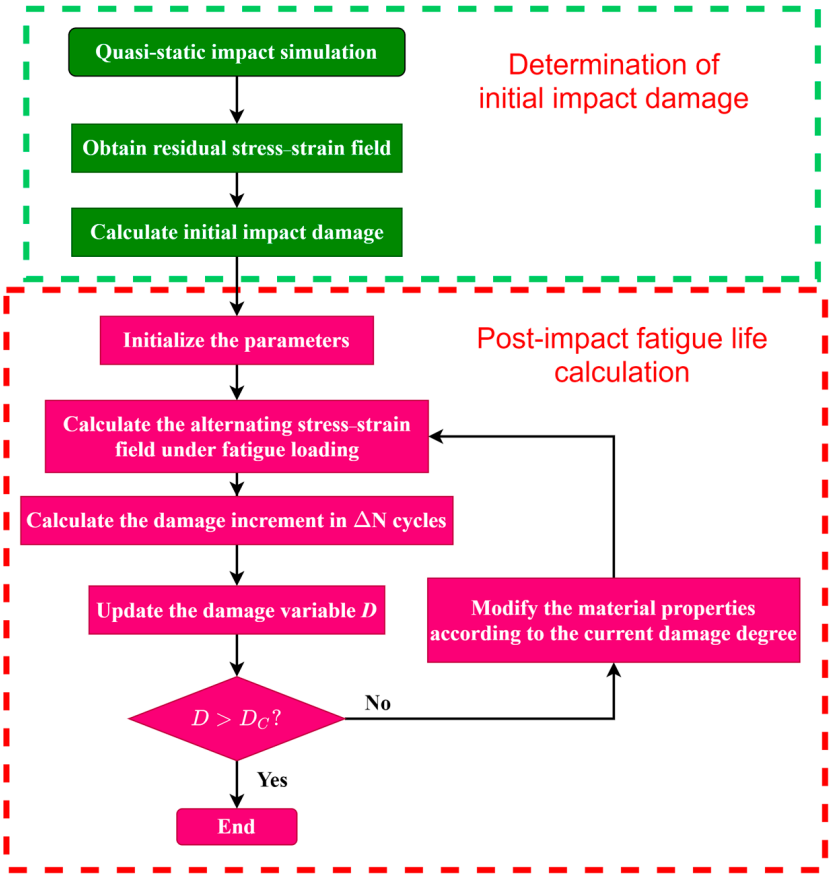

Figure 8. Flowchart for post-impact fatigue problem analysis.

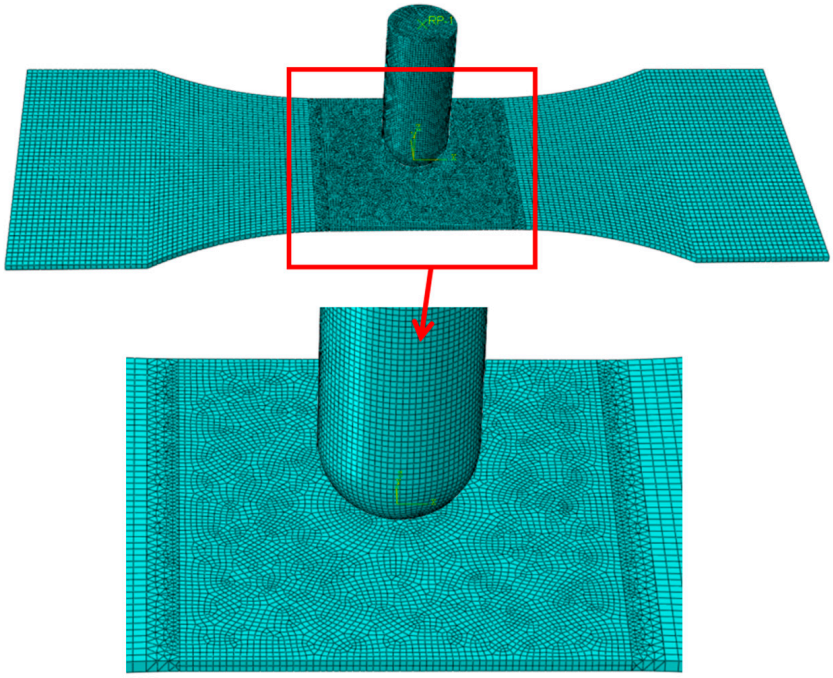

Figure 9. Finite element model for impact.

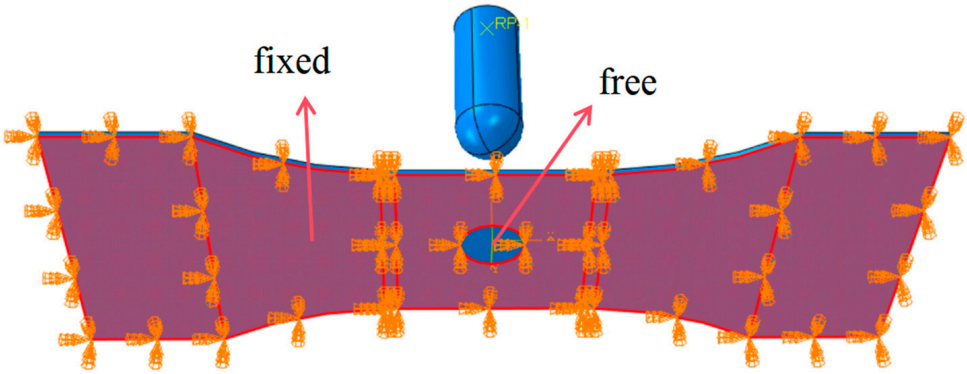

Figure 10. Schematic diagram of boundary condition.

Figure 11 presents the residual stress distribution and residual strain distribution at three different impact depths. It can be seen that the maximum residual stress of the specimen decreases from 346.3 MPa to 202.7 MPa and the maximum residual strain increases from 0.0944 to 0.1593 as the depth of the impact pit increases. When the hammer impacts the specimen, the specimen yields and enters the plastic stage, at which time the maximum Mises stresses at the three impact pit depths are almost the same, because the stress–strain curve of the material is nearly horizontal after entering the plastic stage. After the hammer is out of contact with the specimen, a portion of the specimen's deformation recovers, resulting in some relaxation of the Mises stress. In the case studied in this paper, as the depth of the impact pit increases, the more the Mises stress relaxes; therefore, the maximum residual Mises stress after impact is smaller. Figure 12 shows the residual stresses along the impact direction and the length direction of the specimen for the three impact pit depths. It can be found that as the impact pit depth increases, the compressive stress in the length direction of the specimen decreases while the compressive stress in the impact direction increases. The maximum residual strain occurs at the bottom of the impact pit for all three cases. When the impact depth is small, the maximum residual stress is observed at the bottom of the impact pit, whereas it shifts to the junction between the free and fixed surfaces at larger depths.

After obtaining the residual stress–strain field, the initial impact damage was calculated using Lemaitre's elastic–plastic damage evolution equation, and the maximum initial impact damage for different impact pit depths is listed in Table 7.

5.2. Post-Impact Fatigue Life Prediction

After the impact was completed, the fatigue load was applied to the specimen with the impact pit. One end of the specimen was fixed, and an alternating load was applied to the other end, as shown in Figure 13. The USDFLD subroutine was written to implement damage accumulation. The post-impact fatigue life was then calculated by considering the combined effects of impact pit and fatigue load. For the specimen without an impact pit, the peak load was maintained at 36 kN, which is consistent with the experimental loading condition. The damage distribution of the specimen and the damage accumulation curve of the critical element are presented in Figure 14. It can be seen that the location of the largest damage occurs at the boundary between the transition section and the smooth section due to a minor stress concentration. The calculated life of the specimen is 144,000, with a relative error of less than 6% compared to the experimental life.

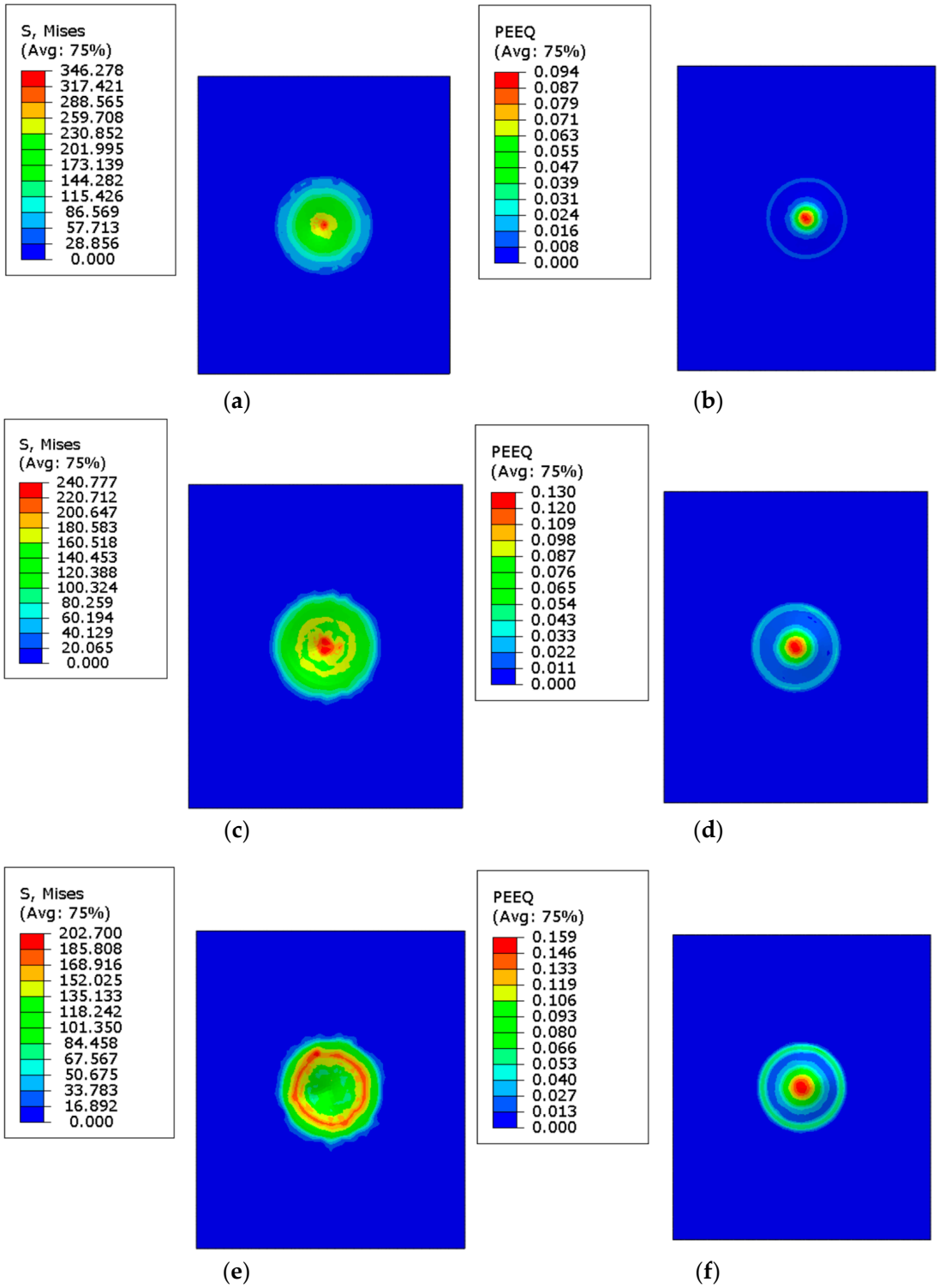

Figure 11. Residual stress–strain field distribution in the vicinity of the impact pit; (**a**,**c**,**e**) residual stress distribution for impact pit depths of 0.67 mm, 1.33 mm, and 2 mm, respectively; (**b**,**d**,**f**) residual plastic strain distribution for impact pit depths of 0.67 mm, 1.33 mm, and 2 mm, respectively.

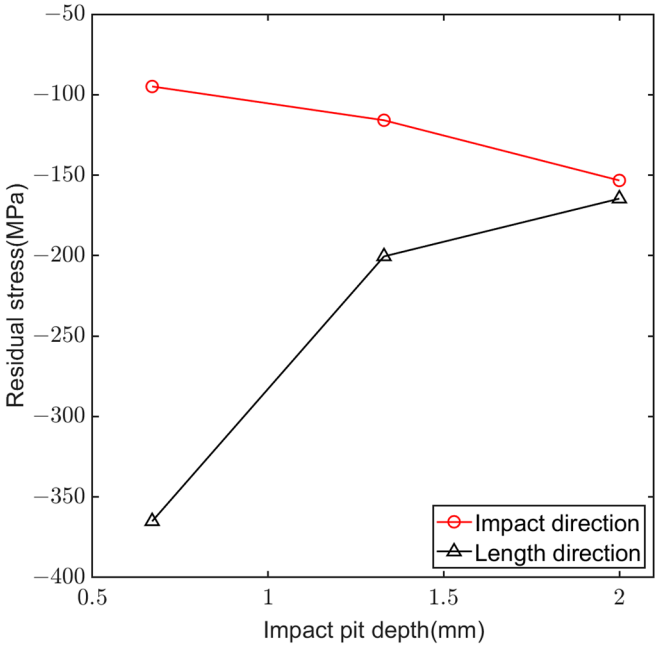

Figure 12. Residual stresses along the direction of impact and the length of the specimen.

Table 7. Maximum initial impact damage at different impact pit depths.

Impact pit depth/mm	0.67	1.33	2.0
Maximum initial impact damage	0.0104	0.0217	0.0382

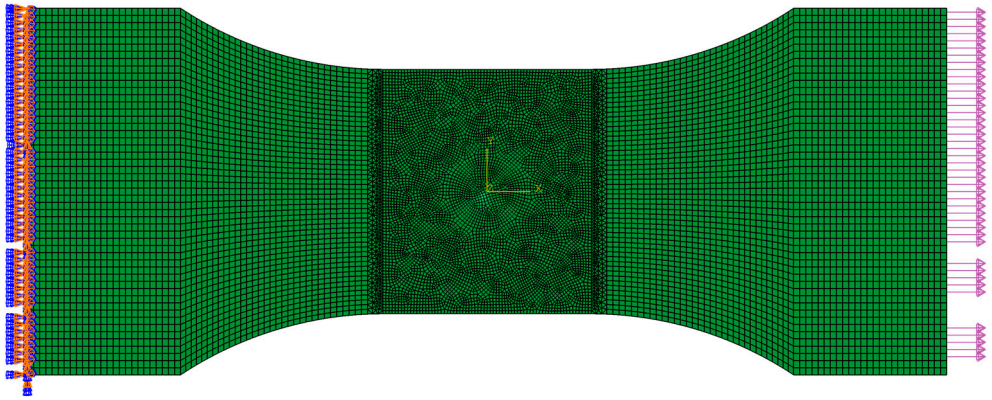

Figure 13. Finite element model for post-impact fatigue life prediction.

The peak loads for impact pit depths of 0.67 mm, 1.33 mm, and 2 mm were 28 kN, 25 kN, and 22 kN, respectively, and the stress ratios were 0.06 for the three cases, which also coincided with the experimental conditions. Figure 15 presents the damage distribution in the vicinity of the impact pit for the three cases, revealing that the critical elements are distributed in a long strip perpendicular to the direction of load application. Figure 16 shows the damage accumulation curves for the critical elements at three impact pit depths. The damage increases exponentially with the number of loading cycles, and the damage accumulates slowly in the early stage, while it grows rapidly in the later stage. The damage accumulates from 0.0104, 0.0217, and 0.0382 at a cycle number of 0 for impact pit depths of 0.67 mm, 1.33 mm, and 2 mm, respectively, and the number of cycles at which the damage accumulates to the critical value (taken as 0.95 in the numerical simulation) is 212,000, 156,000, and 138,000 for the three cases, respectively. The comparison between

the calculated lives and the experimental lives is given in Figure 17, from which it can be found that none of the calculated lives fall outside the twice error band, demonstrating the feasibility of the methodology in this study.

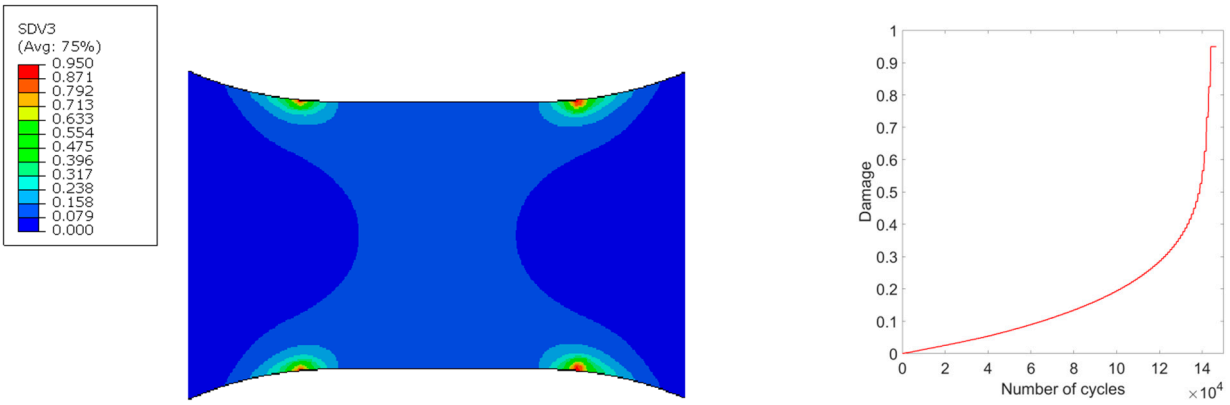

Figure 14. Damage distribution and damage accumulation curve for the specimen without impact pit, (**a**) damage distribution; (**b**) damage accumulation curve.

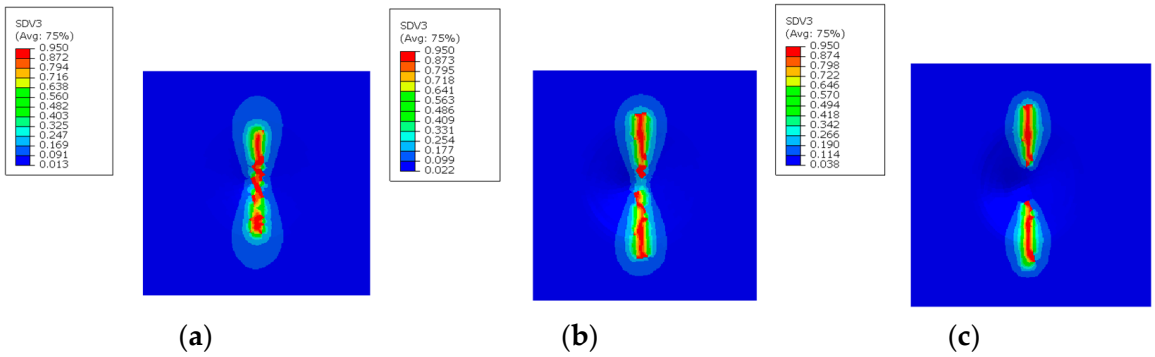

Figure 15. Damage distribution of the specimens with impact pits at three different pit depths, (**a**) depth = 0.67 mm; (**b**) depth = 1.33 mm; and (**c**) depth = 2 mm.

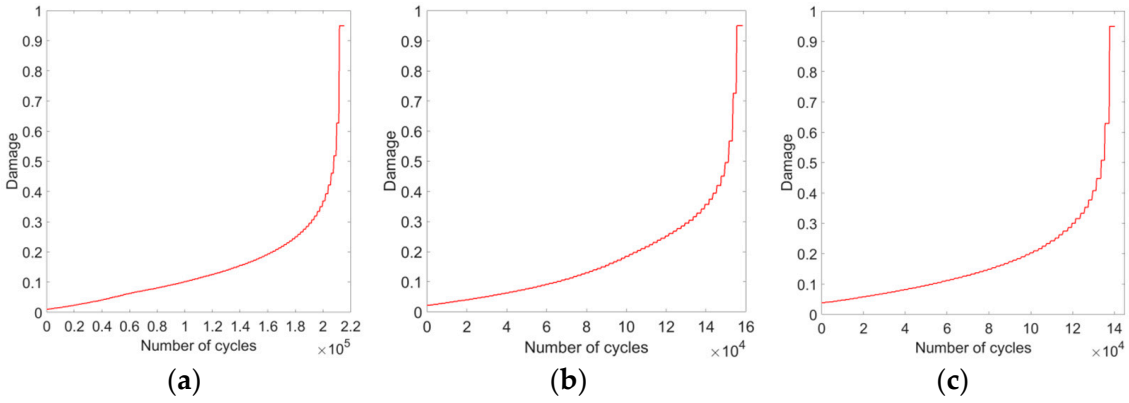

Figure 16. Damage accumulation curves of the specimens with impact pits at three different pit depths, (**a**) depth = 0.67 mm; (**b**) depth = 1.33 mm; and (**c**) depth = 2 mm.

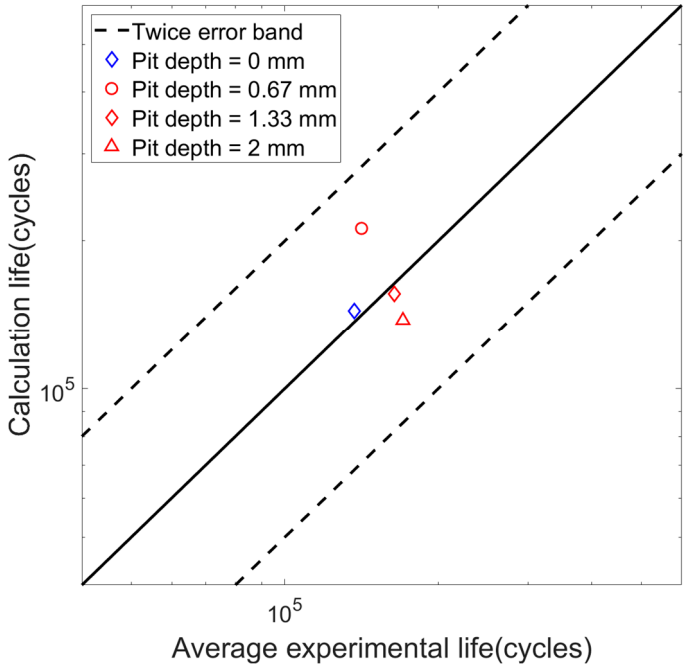

Figure 17. Comparison between the calculation results and the experimental results.

6. Conclusions

The post-impact fatigue life of the 2060 aluminium–lithium alloy plate is predicted based on the damage mechanics method, and the main conclusions are as follows:

1. A fatigue test was carried out on the specimens with impact pits. The experimental results elucidate that impact loading engenders a considerable proliferation of micro-cracks, serving as nucleation sites for subsequent fatigue crack propagation. The heightened density of these micro-cracks significantly facilitates the initiation and advancement of the main crack.
2. The theoretical models for the analysis of post-impact fatigue problems were established. Based on the theory of continuum damage mechanics, the plastic damage evolution model and the elastic damage evolution model are used to calculate the initial impact damage and fatigue damage, respectively.
3. A quasi-static impact simulation was carried out to obtain the residual stress–strain field of the specimen after impact. The calculation results show that the maximum residual stress of the specimen decreases while the maximum residual strain increases with the increase in the impact pit depth.
4. The initial impact damage was determined according to Lemaitre's plastic damage evolution equation. The initial damage becomes larger as the depth of the impact pit increases. The post-impact fatigue life of the specimens was predicted by considering the combined effect of the impact pit and fatigue load. The calculation results are in good agreement with the experimental results, which verifies the effectiveness of the method in this study.

Author Contributions: Conceptualization, L.L. and X.L.; Experiment, L.L.; Methodology, L.L. and Z.Z.; Software, X.L.; Validation, L.L. and Z.Z.; Formal Analysis, L.L. and X.L.; Investigation, L.L., X.L. and Z.Z.; Resources, Z.Z., W.H. and Q.M.; Data Curation, X.L.; Writing—Original Draft Preparation, L.L., X.L. and Z.Z.; Writing—Review and Editing, Z.Z., W.H. and Q.M.; Visualization, Z.Z.; Supervision, Z.Z. and Q.M.; Project Administration, Z.Z. All authors have read and agreed to the published version of the manuscript.

Funding: This research received no external funding.

Conflicts of Interest: The authors declare no conflicts of interest.

References

1. Yu, N.H.; Shang, J.Z.; Cao, Y.J.; Ma, D.X.; Liu, Q.M. Comparative Analysis of Al-Li Alloy and Aluminum Honeycomb Panel for Aerospace Application by Structural Optimization. *Math. Probl. Eng.* **2015**, *2015*, 815257. [CrossRef]
2. Ahmed, B.; Wu, S. Aluminum lithium alloys (Al-Li-Cu-X)-New generation material for aerospace applications. *Appl. Mech. Mater.* **2014**, *440*, 104–111. [CrossRef]
3. Alexopoulos, N.D.; Migklis, E.; Stylianos, A.; Myriounis, D.P. Fatigue behavior of the aeronautical Al-Li(2198) aluminum alloy under constant amplitude loading. *Int. J. Fatigue* **2013**, *56*, 95–105. [CrossRef]
4. Karayan, I.A.; Jata, K.; Velez, M.; Castaneda, H. On exfoliation corrosion of alloy 2060 T8E30 in an aggressive acid environment. *J. Alloys Compd.* **2016**, *657*, 546–558. [CrossRef]
5. Yu, Y.B.; Chen, L.P.; Xu, Y.; Yuan, Y.P.; Fang, S.P. High temperature tensile deformation behaviour and microstructure of 2060-T8E30 aluminium-lithium alloy. *Mater. Rep.* **2023**, *37*, 119–124. (In Chinese)
6. Rioja, R.J.; Liu, J. The evolution of Al-Li base products for aerospace and space applications. *Metall. Mater. Trans. A* **2012**, *43*, 3325–3337. [CrossRef]
7. Dursun, T.; Soutis, C. Recent developments in advanced aircraft aluminium alloys. *Mater. Des.* **2014**, *56*, 862–871. [CrossRef]
8. Williams, C.J., Jr. SAE. Progress in structural materials for aerospace systems. *Acta Mater.* **2003**, *51*, 5775–5799. [CrossRef]
9. Liu, X.C.; Xi, X.L.; Bai, C.Y.; Yang, J.L.; Yang, X.F. Dynamic response and failure mechanism of Ti-6AL-4V hi-lock bolts under combined tensile-shear loading. *Int. J. Impact Eng.* **2019**, *131*, 140–151. [CrossRef]
10. Gupta, A.; Bennett, C.J.; Sun, W.; Neate, N. On the microstructural evolution and failure mechanism in laser powder bed fusioned Ti–6Al–4V during low cycle fatigue at room and elevated temperatures. *J. Mater. Res. Technol.* **2022**, *21*, 4299–4319. [CrossRef]
11. Chowdhury, S.; Zabel, V. Stochastic selection of fatigue crack growth model for a damaged bridge gusset plate. *Int. J. Fatigue* **2023**, *173*, 107674. [CrossRef]
12. Giglio, M.; Beretta, S.; Mariani, U.; Ratti, G. Defect tolerance assessment of a helicopter component subjected to multiaxial load. *Eng. Fract. Mech.* **2010**, *77*, 2479–2490. [CrossRef]
13. Lazzeri, L.; Mariani, U. Application of damage tolerance principles to the design of helicopters. *Int. J. Fatigue* **2009**, *31*, 1039–1045. [CrossRef]
14. Cheng, Z.Q.; Xiong, J.J.; Tan, W. Fatigue crack growth and life prediction of 7075-T62 aluminium-alloy thin-sheets with low-velocity impact damage under block spectrum loading. *Int. J. Fatigue* **2022**, *155*, 106618. [CrossRef]
15. Liu, X.; Zheng, G.; Luo, Q.; Li, Q.; Sun, G. Fatigue behavior of carbon fibre reinforced plastic and aluminum single-lap adhesive joints after the transverse pre-impact. *Int. J. Fatigue* **2020**, *144*, 105973. [CrossRef]
16. Zhan, Z.; Hu, W.; Shen, F.; Meng, Q.; Pu, J.; Guan, Z. Fatigue life calculation for a specimen with an impact pit considering impact damage, residual stress relaxation and elastic-plastic fatigue damage. *Int. J. Fatigue* **2017**, *96*, 208–223. [CrossRef]
17. Yang, S.; Hu, W.; Li, J.; Meng, Q.; Zhan, Z. Fatigue tests and damage model development on Al-Si-Mg aluminum alloys with low-velocity impact pit. *Int. J. Fatigue* **2021**, *153*, 106466. [CrossRef]
18. Fleury, R.M.N.; Salvati, E.; Nowell, D.; Korsunsky, A.M.; Silva, F.; Tai, Y.H. The effect of surface damage and residual stresses on the fatigue life of nickel superalloys at high Temperature. *Int. J. Fatigue* **2019**, *119*, 34–42. [CrossRef]
19. Boyce, B.; Chen, X.; Peters, J.; Hutchinson, J.W.; Ritchie, R.O. Mechanical relaxation of localized residual stresses associated with foreign object damage. *Mater. Sci. Eng. A* **2003**, *349*, 48–58. [CrossRef]
20. Chen, Y.; Ji, C.; Zhang, C.; Wang, F.; Song, X. Analysis for post-impact tensile-tensile fatigue damage of 2024-T3 sheets based on tests, digital image correlation (DIC) technique and finite element simulation. *Int. J. Fatigue* **2019**, *122*, 125–140. [CrossRef]
21. Zhang, X.Y.; Cui, Z.F.; Pan, X.C.; Chen, Z.; Dong, T.J.; Chen, Y.J. *Post-Impact Fatigue Performance of 2198-T8 Aluminum-Lithium Alloy Sheet with Pre-Crack*; Engineering Technology Training Center, Civil Aviation University of China: Tianjin, China, 2023; p. 51.
22. Huang, W.; Sun, L.; Li, L.; Shen, L.; Huang, B.; Zhang, Y. Investigations on low-energy impact and post-impact fatigue of adhesively bonded single-lap joints using composites substrates. *J. Adhes.* **2019**, *96*, 1326–1354. [CrossRef]
23. Chen, Y.J.; Yang, J.C.; Peng, J.S.; Ji, C.; Wang, B. Low-velocity impact (LVI) and post-impact fatigue properties of GLARE laminates with holes. *Int. J. Fatigue* **2023**, *167*, 107318. [CrossRef]
24. Rogani, A.; Navarro, P.; Marguet, S.; Ferrero, J.F. Study of post-impact behaviour of thin carbon/epoxy laminates subject to fatigue tensile loading. *Int. J. Fatigue* **2021**, *148*, 106134. [CrossRef]
25. Yang, S.; Hu, W.; Meng, Q.; Zhao, B. A new continuum damage mechanics-based twoscale model for high-cycle fatigue life prediction considering the two-segment characteristic in S-N curves. *Fatigue Fract. Eng. Mater. Struct.* **2020**, *43*, 387–402. [CrossRef]
26. Shen, F.; Hu, W.; Meng, Q. A damage mechanics approach to fretting fatigue life prediction with consideration of elastic-plastic damage model and wear. *Tribol. Int.* **2015**, *82*, 176–190. [CrossRef]
27. Shen, F.; Hu, W.; Voyiadjis, G.Z.; Meng, Q. Effects of fatigue damage and wear on fretting fatigue under partial slip condition. *Wear* **2015**, *338–339*, 394–405. [CrossRef]
28. Hu, P.; Meng, Q.; Hu, W.; Shen, F.; Zhan, Z.; Sun, L. A continuum damage mechanics approach coupled with an improved pit evolution model for the corrosion fatigue of aluminum alloy. *Corros. Sci.* **2016**, *113*, 78–90. [CrossRef]
29. Wang, X.J.; Meng, Q.C.; Hu, W.P. Continuum damage mechanics-based model for the fatigue analysis of welded joints considering the effects of size and position of inner pores. *Int. J. Fatigue* **2020**, *139*, 105749. [CrossRef]
30. Xu, Z.Z.; Li, Y.; Zhang, Y.D. Segregation behavior of 2060 Al-Li alloy during twin roll casting. *Nonferrous Met. Eng.* **2024**, *14*, 32–42. (In Chinese)

31. Murakami, S. *Continuum Damage Mechanics: A Continuum Mechanics Approach to the Analysis of Damage and Fracture*; Springer Science & Business Media: Berlin/Heidelberg, Germany, 2012.
32. Lemaitre, J.; Desmorat, R. *Engineering Damage Mechanics: Ductile, Creep, Fatigue and Brittle Fatigue*; Springer: Berlin/Heidelberg, Germany, 2005.
33. Xiao, Y.C.; Li, S.; Gao, Z. A continuum damage mechanics model for high cycle fatigue. *Int. J. Fatigue* **1998**, *20*, 503–508. [CrossRef]
34. Shen, F.; Hu, W.P.; Meng, Q.C.; Zhang, M. A new damage mechanics based approach to fatigue life prediction and its engineering application. *Acta Mech. Solida Sin.* **2015**, *28*, 510–520. [CrossRef]